nature communications

Article

https://doi.org/10.1038/s41467-026-70910-5

Smallest acyclic tricationic molecule containing a Bis(phosphine)-stabilized low-valent triantimony-based Unit

Received: 5 September 2025

Accepted: 5 March 2026

Published online: 21 March 2026

Check for updates

Nilanjana Mukherjee[1], Benjamin Peerless[2], Vincent L. Nadurata[2], Vikas Kumar[1], Mayur P. Sangole[3], Kirandeep Singh[3], Haakon T. A. Wiedemann[4], Christopher W. M. Kay[4,5], Robert Kruk[2], Florian Weigend[6] ✉, Stefanie Dehnen[2] ✉, Rajesh G. Gonnade[3] ✉, Cem B. Yildiz[7] ✉ & Moumita Majumdar[1] ✉

Element-element bonded multiply charged cationic species are well known as dimers or small cyclic oligomers in the condensed phase. However, the smallest acyclic version, a trinuclear unit possessing greater than a mono-cationic charge, has remained elusive. Here we introduce a bis(phosphine) supported low valent triantimony-based tricationic compound as a new entrant in this field. Structural elucidation and electronic understanding reveal a W-shaped tricationic unit comprising of a three-center four-electron sigma-bonded triantimony moiety that is terminally capped by bis(phosphine) ligands, with the central antimony atom having two lone pairs of electrons. The unique counter trianion $[Sb(O)_2(OTf)_4]^{3-}$ (OTf = CF_3SO_3) possesses reactive polar $Sb^{\delta+}$–$O^{\delta-}$ bonds, the structure of which is determined from single crystal X-ray diffraction analysis. The ensemble of reactive molecular fragments found in this highly charged antimony-based compound makes it thermally unstable. Nonetheless, this fully characterized fleeting species shows a diverse reactivity profile, advancing the isolation of various novel antimony compounds, including the formation of a distinct low-valent antimony-cobalt carbonyl cluster.

Stabilization of reactive main group species in the condensed phase has comprehensively enriched our understanding of reaction intermediates and chemical bonding[1,2]. Among them, stabilization of multiply charged ions[3] is at the forefront of contemporary research. The seminal report on dihelium dication He_2^{2+} by Pauling in 1933[4] marked the gateway to multiply charged ions as important species found not only in interstellar medium[3], but also as key intermediates in chemical reactions and materials[5]. In the condensed phase, multiply charged ions with distantly charge-separated scaffolds having long-range electrostatic interactions or large-sized clusters and Zintl ions having delocalized systems mitigate the intramolecular Coulombic repulsions[6] and are thus recognized as stable species[7,8]. On contrary, syntheses of element-element bonded multiply charged molecules has remained an arduous task due to strong electrostatic repulsive forces

[1]Department of Chemistry, Indian Institute of Science Education and Research, Pune, Dr. Homi Bhabha Road, Pashan, Pune, Maharashtra, India. [2]Karlsruhe Institute of Technology, Institute of Nanotechnology, Hermann-von-Helmholtz Platz 1, Eggenstein-Leopoldschafen, Germany. [3]CSIR-National Chemical Laboratory, Pune, Maharashtra, India. [4]Saarland University, Saarbrücken Campus, Saarbrücken, Germany. [5]London Centre for Nanotechnology, University College London, 17-19 Gordon Street, London, United Kingdom. [6]Karlsruhe Institute of Technology, Institute for Quantum Materials and Technologies, Eggenstein-Leopoldschafen, Germany. [7]Bartin University, Faculty of Engineering, Architecture and Design, Department of Basic Sciences, Bartın, Türkiye. ✉e-mail: florian.weigend@kit.edu; stefanie.dehnen@kit.edu; rg.gonnade.ncl@csir.res.in; cbyildiz@bartin.edu.tr; moumitam@iiserpune.ac.in

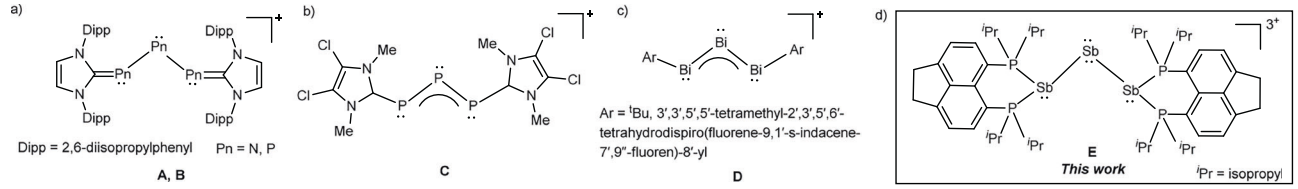

Fig. 1 | Examples of ligand-supported low-valent trinuclear-based cationic compounds. a *N*-Heterocyclic carbene-supported $\{N_3\}$- and $\{P_3\}$-based cations (**A** and **B**). **b** *N*-Heterocyclic carbene-stabilized $\{P_3\}$-based cation (**C**). **c** Trimetallic bismuth(I)-based monocation (**D**). **d** Trication based on a bis(phosphine)-stabilized acyclic triantimony unit (**E**, this work).

leading to electron loss or molecular fragmentation, known as Coulombic explosion[6].

Suitable combination of weakly coordinating anions and appropriate ligands capable of dispersing the charge density have led to the successful stabilization of Group 13–15 homoatomic dicationic dimers[9–16] and multiply charged cationic clusters (cyclic tri-/tetra-/pentamers)[9,17–19], overcoming their intramolecular Coulombic repulsions. Recently, a supramolecular stabilization approach was introduced for a formally tetracationic Bi_4^{4+} ring[20]. Notably, there are only two examples known in literature thus far on the syntheses of dimers possessing even higher charges, including our recent report on a bis(α-iminopyridine) stabilized-distibane tetracation[21,22]. There is precedence for a few acyclic trimers featuring three contiguously bonded atoms in low oxidation state, however, with only overall monopositive charge (Fig. 1a–d)[23–26]. Unlike the cyclic analogues, acyclic trinuclear-based compounds possessing an overall tricationic charge have remained elusive. However, it is worth mentioning that gas phase investigations show the formation of highly reactive tricationic trinuclear species such as $(CO_2)^{3+}$ ions or the allene trication[27–29]. Despite the limited knowledge of such species, it could be envisaged that the isolation of heavier element-based species would be more attainable as they are intrinsically capable of accumulating multiple charges owing to the larger atomic sizes.

Herein we present the synthesis, characterization, and reactivity of a unique low-valent triantimony-based tricationic molecule in the ionic compound **1** (Fig. 1E) stabilized by two bis(phosphine) molecules at the terminal antimony sites. In conjunction, we introduce an unusual antimony(V)-dioxo-based trianion, maintaining the overall charge neutrality of **1**. Single-crystal X-ray diffraction analysis and electronic structure calculations reveal the presence of a covalently bonded acyclic and bent Sb–Sb–Sb unit. The dicoordinated central Sb atom possesses two lone pairs of electrons, while the terminal Sb centers of the trimetallic unit carry one lone pair of electrons each. We additionally present reactivity studies of **1** that demonstrate the lability of the Sb–Sb bond and the strong influence of the counter trianion.

Results and discussion

Synthesis and structure determination

The low-valent triantimony-based tricationic compound **1** coordinated by 5,6-bis(diisopropylphosphino)acenaphthene (L) at the terminal Sb centers along with its unique $[Sb(O)_2(OTf)_4]^{3-}$ counter trianion (OTf = CF_3SO_3) was obtained from the reaction between [LSb](OTf) and $Sb(OTf)_3$. The reactants were combined in a 3:1 ([LSb](OTf): $Sb(OTf)_3$) ratio in dichloromethane and maintained at −35 °C (Fig. 2a). [LSb](OTf) was reported by us; it shows the ability of the Sb(I) center coordinating to coinage metal ions[30]. $Sb(OTf)_3$ was prepared following a literature procedure[18]. Intensely red-colored single crystals of **1** were grown from a dichloromethane solution at −35 °C. Compound **1** is thermally labile. Upon warming to room temperature, a rapid fading of the solution color to orange, along with precipitation of metallic Sb was observed. Single crystals grown by layering this pale orange colored dichloromethane solution with pentane, gave an Sb-O-Sb based compound, **2** [LSb−O−Sb$(OTf)_4$] (Fig. 2a) as a white crystalline solid (*vide infra*).

In-situ generation of **1** in CD_2Cl_2 and CD_3CN at 243 K was studied by NMR spectroscopy (Figure S2, S9 and S10). The $^{31}P\{^1H\}$ NMR spectra showed a peak at +17.2 ppm in CD_3CN and one at +13.4 ppm in CD_2Cl_2, assigned to **1**. There were additional peaks present arising from L, protonated $[LH_2](OTf)_2$, and the diphosphonium dication $L(OTf)_2$, indicating the involvement of redox processes. The presence of peaks due to phosphine oxides indicated the influence of inadvertent moisture, likely from the $Sb(OTf)_3$ precursor. Amongst these side products formed, compound **1** was calculated to be present in 15%, using triphenyl phosphate as internal NMR standard (Figure S8). Variable-temperature coupled with time-dependent $^{31}P\{^1H\}$ NMR data showed the instability of **1** (*vide infra*). Absorbance data in acetonitrile reveals a maximal absorption (λ_{max}) at 418 nm ($\varepsilon = 1030.83\ M^{-1}\ cm^{-1}$) and a broad shoulder at 500 nm (Figure S32–S33). The collection of single-crystal X-ray diffraction data of sufficient quality for structure solution and refinement was achieved for **1** after numerous attempts.

Compound **1** crystallizes in the centrosymmetric monoclinic space group *C*2/*c*, featuring half of the tricationic fragment and half of the trianionic unit $[Sb(O)_2(OTf)_4]^{3-}$ in the asymmetric unit (Fig. 2b, c). Altogether, the cation in **1** possesses a W-shaped conformation. The central antimony atoms, Sb2 (cationic unit) and Sb3 (anionic unit) lie on a two-fold rotation axis, which generates the remaining half fragment of both the cationic and anionic moieties by symmetry (Table S19). The triantimony $\{Sb_3\}$ unit has a Sb1–Sb2 bond length of 2.7735(8) Å and bent angle of 87.42(3)° at the central Sb2. The P1–Sb1 and P2–Sb1 bond lengths are 2.556(3) Å and 2.572(2) Å, respectively, noticeably elongated compared to those present in [LSb](OTf) (Sb1–P1 2.4595(9) Å, Sb1–P2 2.4598(9) Å)[30]. The distance between the two terminal Sb atoms is 3.833(9) Å, falling within the sum of their van der Waals radii (4.40 Å)[31]. Relatable bent $\{Sb_3\}$ units are present in $[Sb_3Ph_4]^-$ and $[Sb(Sb^tBu_2)_2]^-$ anions [32,33].

The counter-trianion is based on an SbO_2 core, with four triflate units bound to the central Sb(V) atom (Fig. 2c), resembling the acetate salt of uranium oxide[34]. The triflate units of $[SbO_2(OTf)_4]^{3-}$ display thermal disorder over two positions with roughly 70% and 30% occupancies. Nonetheless, the discernible Sb3-O5(OTf) bond length is 2.175(9) Å. The Sb3-O1 bond length is 1.834(13) Å, close to that reported for monomeric stibine oxide (Sb=O distance being 1.837(2) Å)[35]. Such bonds may be understood as a polar, $Sb^{\delta+}–O^{\delta-}$ rather than Sb=O, due to the large differences in atomic sizes and electronegativities between Sb and O atoms[36]. The presence of an '$O^{\delta-}=Sb(V)^{\delta++}=O^{\delta-}$'unit in the anion of **1** devoid of any steric protections is probably responsible for the thermal instability. A similar thermal instability was reported for $Dipp_3Bi^{\delta+}–O^{\delta-}$ (Dipp = 2,4,6-diisopropylphenyl)[37]. The unstable trianion in **1** loses one oxygen atom, manifesting in the formation of **2**. Despite numerous efforts, anion exchange (PF_6, SbF_6, $B(C_6F_5)_4$ anions) in **1** was not successful, each time leading to **2**.

Compound **2** crystallizes in the centrosymmetric monoclinic space group $P2_1/c$ (Table S19). The molecular structure of **2** has a bent Sb1–O1–Sb2 core, with different substituents on the two Sb centers (Fig. 2d). Sb1 is coordinated by the phosphine ligand, adopting a

https://doi.org/10.1038/s41467-026-70910-5

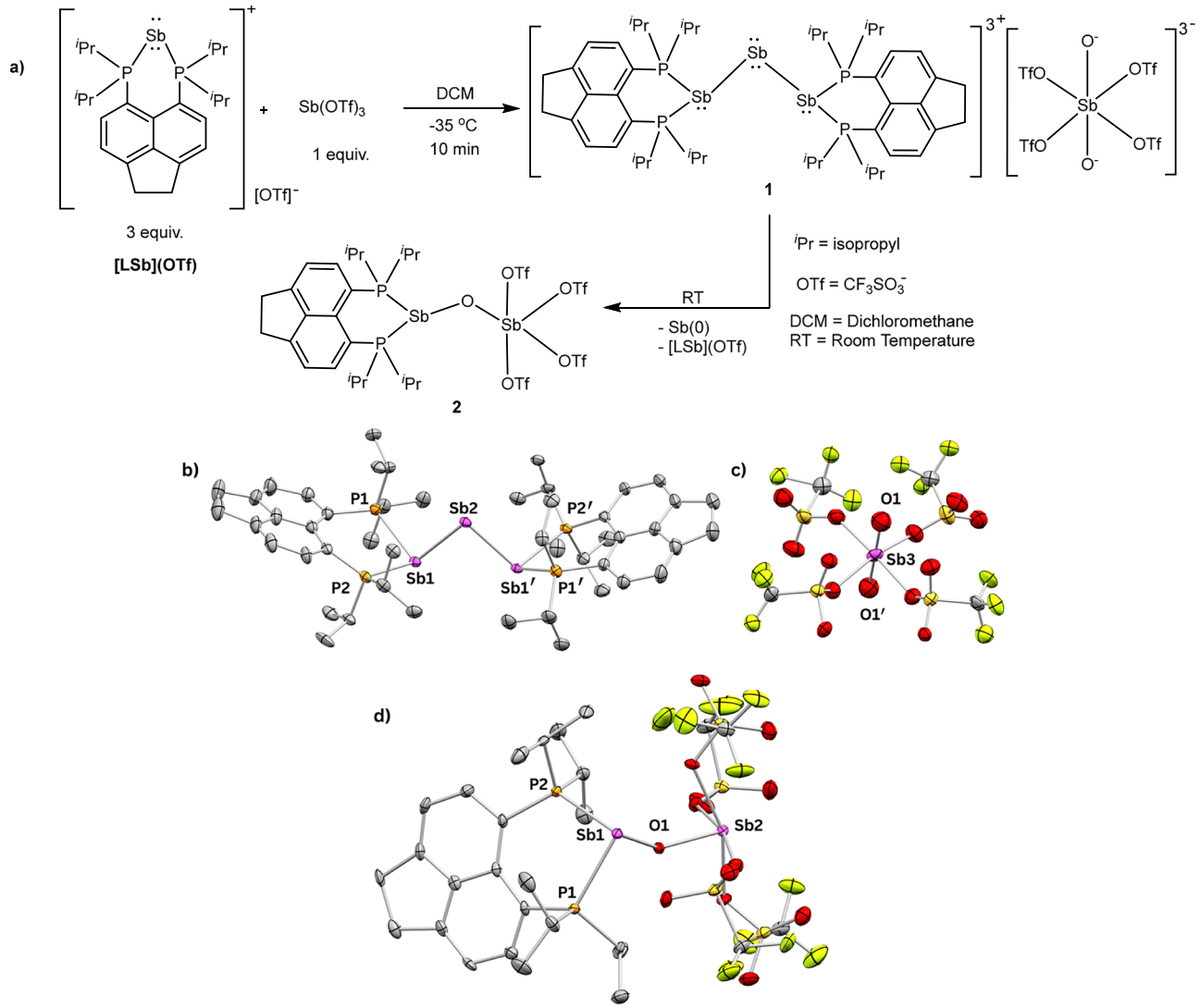

Fig. 2 | Syntheses and ORTEPs of bis(phosphine)-stabilized triantimony-based tricationic molecule 1 and oxo-bridged diantimony compound 2. a Synthesis of **1** by using three equivalents of [LSb](OTf) and one equivalent of $Sb(OTf)_3$ and its subsequent conversion to **2**; **b** Molecular structure of $[L_2Sb_3]^{3+}$ in the solid-state structure of **1** (thermal ellipsoids at 35%, H atoms are omitted for clarity), Selected bond lengths [Å] and angles [°]: P1–Sb1 2.556(3), P2–Sb1 2.572(2), Sb1–Sb2 2.7735(8); P1–Sb1–P2 86.27(8), Sb1–Sb2–Sb1′ 87.42(3); **c** Molecular structure of the $[Sb(O)_2(OTf)_4]^{3-}$ counter-trianion in the solid-state structure of **1** (thermal ellipsoids at 35%); **d** Molecular structure of **2** [LSb–O–Sb(OTf)$_4$] in the solid state (thermal ellipsoids at 35%, H atoms, and solvent molecule omitted for clarity), Selected bond lengths [Å] and angles [°]: P1–Sb1 2.588(2), P2–Sb1 2.557(2), Sb1–O1 1.947(3), Sb2–O1 1.928(4); P3–Sb1–P4 87.89(5), Sb1–O1–Sb2 129.7(2). The color code refers to the colors used in the crystal structure figures: Sb (magenta), P (orange), O (red), S (yellow), F (light green), C (gray).

trigonal pyramidal geometry, while Sb2 has a square pyramidal environment with four triflates situated in distorted basal plane. The Sb1–O1 and Sb2–O1 bond lengths are 1.947(3) Å and 1.928(4) Å, respectively with a Sb1–O1–Sb2 angle of 129.7(2)°. The Sb–O–Sb core of **2** is structurally analogous to dimeric stibine oxide $(Ph_3SbO)_2$[38], and related to the triaryl antimony oxide stabilized by a stiborane unit[39]. Infrared stretching frequencies for Sb–O bonds appear at 512 and 575 cm^{-1} (Figure S34)[38].

Insight into the formation of **1** and subsequent conversion to **2** was provided by an in-situ variable temperature (243 K to 298 K) and time-dependent $^{31}P\{^1H\}$ NMR study (Figure S9–S10). We suggest that the reaction involves a reductive catenation process proceeding via initial coordination of [LSb](OTf) to $Sb(OTf)_3$. A simple stoichiometric representation of the reaction between three equivalents of [LSb](OTf) and one equivalent of $Sb(OTf)_3$ for the synthesis of **1** and subsequent conversion to **2** is provided in Figure S11. Beyond the coordinating ability of the bis(phosphine) ligand L, it acts as a $2e^-$ reductant towards Sb with concomitant formation of diphosphonium dication $L(OTf)_2$. The inadvertent presence of water in $Sb(OTf)_3$[18] plays a crucial role in the formation of $[Sb(O)_2(OTf)_4]$ trianion, in conjunction with L as the Brønsted base to give $LH_2(OTf)_2$ (Figure S11). The Sb–Sb bond formed in the $\{Sb_3\}$ unit of **1** is inherently weak due to the large atomic size of Sb. This manifested in the gradual generation of [LSb](OTf) from **1** upon increasing to room temperature from 243 K (Figure S9). The generation of [LSb](OTf) was validated by the addition of its excess into the reaction medium (Figure S19–S20); which did not give rise to any new peak in the in-situ $^{31}P\{^1H\}$ spectra. From the NMR study, it appears **1** has a slightly better stability in CD_3CN compared to CD_2Cl_2 at room temperature, although single crystals of **1** were obtained exclusively from dichloromethane at −35 °C. This conclusion was further bolstered by UV-Vis measurements which reflected the instability of **1** in dichloromethane. The highly reactive $[Sb(O)_2(OTf)_4]$ trianion led to the conversion to **2** within 12 hours in CD_3CN and rapidly in a couple of hours in CD_2Cl_2 at room temperature (Figure S9–S10). The complete disappearance of the peak due to $L(OTf)_2$ suggests its involvement in the oxide transfer process from Sb(V) to form the phosphine oxide[35].

https://doi.org/10.1038/s41467-026-70910-5

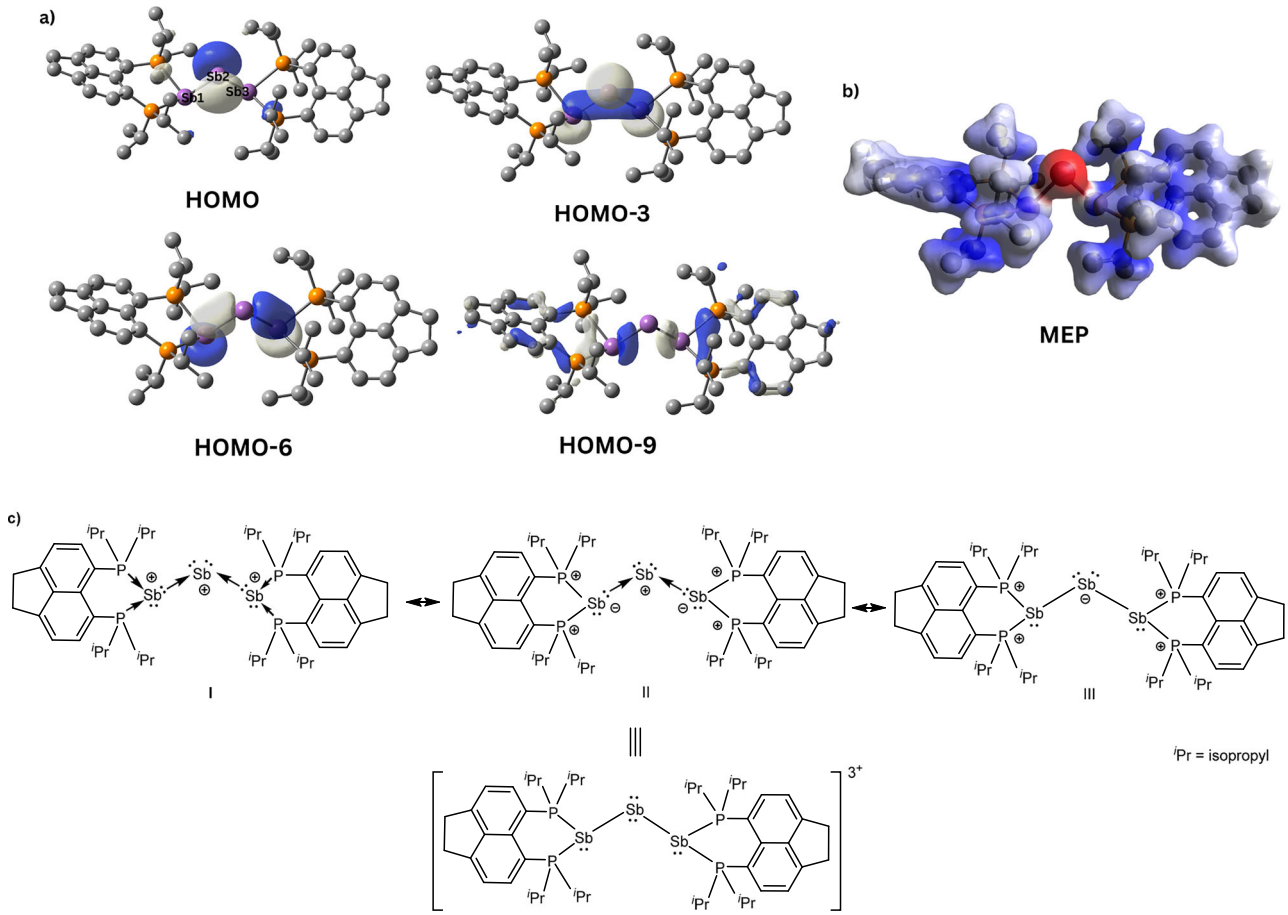

Fig. 3 | Electronic structure of the tricationic bis(phosphine)-stabilized triantimony compound 1. (optimized at BP86-D4/def2-TZVPP level of theory) a Selected Kohn-Sham orbital representations of **1**. **b** Molecular Electrostatic Potential (MEP) map of **1. c** Possible resonance forms of **1**. Note that Sb3 in the computed structure refers to Sb1′ in the crystal structure (see Fig. 2b), owing to the lack of symmetry restrictions in the former.

Various oxides of L formed, as detected in the NMR study, have been rationalized based on experimental (Figure S12–S16) and computational supports (Table S2). Apparently, all free L are ultimately engaged in stabilizing Sb(I) cation or are protonated.

This study demonstrates that **1** represents a rare snapshot during the formation of **2**, the thermodynamically preferred compound. The multi-tasking of L with emphasis on its reducing proficiency makes it indispensable in the trapping of **1**. Ligand substitution of **1** with the chelating ligand 1,2-bis(diphenylphosphino)ethane was not possible, leading only to a rapid conversion to **2** (Figure S26). It is worth mentioning that the formation of **2** was not observed upon the addition of triphenyl phosphine (Figure S22), which is due to its well-known oxygen scavenging ability[35]. While the role of water molecules from the $Sb(OTf)_3$ precursor in the synthesis of **1** has been realized, beyond a certain optimal amount of water, we observe the rapid formation of **2** (Figure S21). The lability of the Sb–Sb bond in **1** is therefore evident from its cleavage in the presence of any external reagents like phosphine or water. Efforts to employ anhydrous $Sb(OTf)_3$ or its derivatives[40,41] or in-situ generated $Sb[B(C_6F_5)_4]_3$ in the preparation of **1** were unsuccessful (Figure S28–S30). Thus, compound **1** stands as the unique smallest acyclic tricationic molecule containing a bis(phosphine)-stabilized $\{Sb_3\}$ unit and an unconventional $[Sb(O)_2(OTf)_4]$ counter trianion.

Computational analysis

The geometric structure of the cationic part in **1** was optimized without symmetry restrictions using the ORCA 5.0.1[42] program package at the BP86-D4/def2-TZVPP level of theory and was confirmed to be the global minimum through frequency calculations. The calculated Sb1–Sb2/Sb2–Sb3 bond length of 2.792 Å, Sb-P (average) length of 2.580 Å and the Sb1–Sb2–Sb3 angle at Sb2 (93°) (Table S3) agree closely with the experimental data (note that Sb3 in the computed structure refers to Sb1′ in the labeling scheme of the crystal structure, owing to the lack of two-fold symmetry restrictions in the former). A Natural Bond Orbital (NBO) analysis of the cation in **1** elucidates that the two terminal Sb1/Sb3 are electronically equivalent and distinct from central Sb2. All three Sb centers feature one non-bonding pair of electrons attributed to the inert $5s^2$-based orbital, corresponding to HOMO-3 (Fig. 3a). The central Sb2 possesses a second lone pair of electrons in a *p*-type orbital, comprising the HOMO (Fig. 3a). HOMO-6 and HOMO-9 show the σ-bonding orbitals between Sb1–Sb2/Sb2–Sb3 (Fig. 3a). Unlike the $\{Bi_3\}$-based monocation[26], the *p*-type lone pair orbital on Sb2 does not undergo suitable orbital overlap for 3c-2e π-bonding. A low positive Laplacian ($\nabla^2\rho$(rBCP) = 0.008) and a low magnitude of electron density (0.059) at the bond critical point (BCP) of Sb1–Sb2 in **1**, obtained from Bader's quantum theory of atoms in molecules (AIM), indicate a weak bonding situation between them (Table S4). The calculated bond dissociation energy (De = 6.6 kcal mol^{-1}) for the reaction $[LSb–Sb–SbL]^{3+} \rightarrow [LSb–Sb]^{2+} + [LSb]^{+}$ reflects the same. Surprisingly, the corresponding calculated Wiberg Bond Order (WBO) value is 1.12 (Figure S35). This discrepancy most likely arises from the strong donor ability of the ligands and presence of lone-pairs on the central Sb atom[43]. The average WBO for Sb–P is 0.75 reflecting single bonds (Table S3). The very low calculated WBO between Sb1 and Sb3 (0.07) and non-covalent interaction studies showing negligible interactions

https://doi.org/10.1038/s41467-026-70910-5

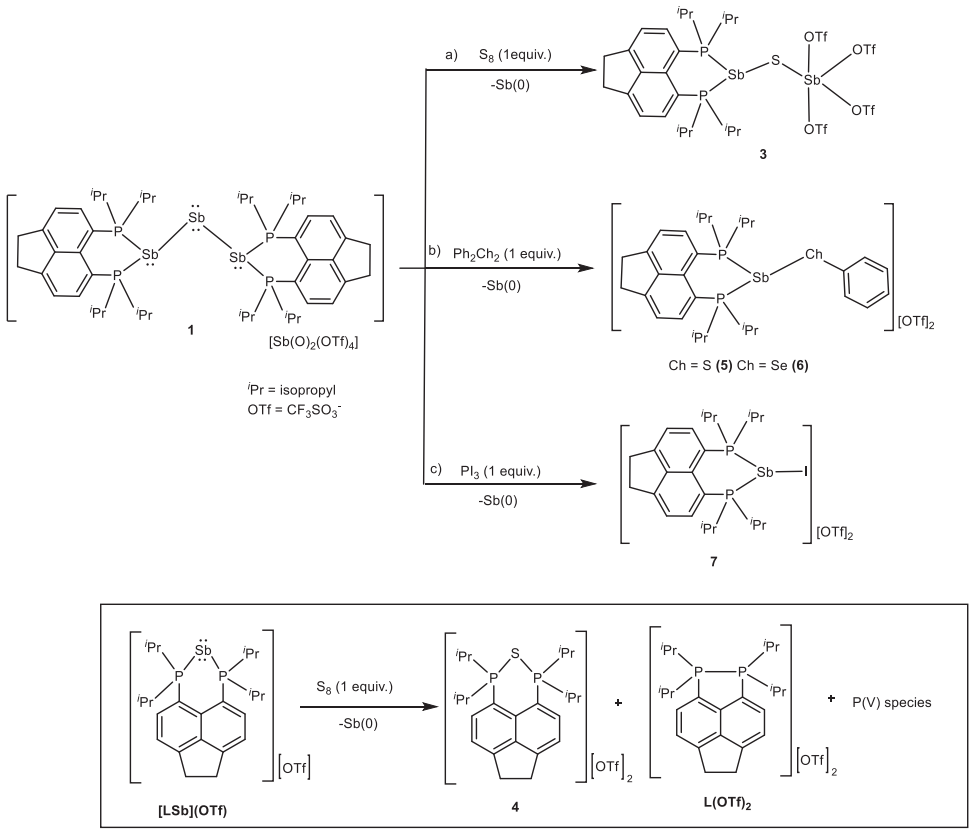

Fig. 4 | Reactivity study with 1 and comparison with the reactivity of [LSb](OTf) in dichloromethane. Reaction of **1** with (**a**) elemental sulfur. **b** Ph_2Ch_2 (Ch = S, Se). **c** PI_3. Inset: Reaction of [LSb](OTf) with S_8.

between the two outer Sb centers (Figure S38) suggest an acyclic $\{Sb_3\}$ molecule. No bond critical point and shared electron density were observed between the two terminal Sb centers of **1** from the AIM and electron localization function (ELF) respectively, reinforcing the acyclic nature of the $\{Sb_3\}$ unit (Figure S36, S37).

Natural Bond Orbital (NBO) charges are +0.28 on the terminal Sb atoms, −0.25 on the central Sb2 and +1.12 on the P atoms (Table S5). A molecular electrostatic potential map shows the positive charges being localized on the terminal antimony atoms and on the coordinating P atoms (Fig. 3b), while the central antimony is negatively charged. Based on this charge analysis, $[L_2Sb_3]^{3+}$ in **1** is closest to the canonical structure III (Fig. 3c). Calculated[44] excitations from Time-Dependent Density Functional Theory (TDDFT) for **1** closely match with the experimental values (Table S7). The lowest excitation (calculated: 519 nm, measured: ~500 nm) is the electronic transition from HOMO (lone pair at the central Sb) to LUMO. The measured peak at ~418 nm stems from two excitations (calculated at 415 nm and 444 nm) of similar oscillator strength, both from the HOMO to low lying unoccupied orbitals (LUMO + 2, LUMO + 4, LUMO + 6). The LUMOs involve the *p* orbitals of the two terminal Sb atoms and that of the neighbored P atoms in antibonding manner (Table S7).

Similar investigations were done[44] for the anionic part with the same settings but additionally employing the conductor-like screening model[45]. Localized MOs[46] (Figure S39) reveal one sigma bond for each of the two axial Sb-O bonds, involving the p_z(O) orbitals as well as p_z(Sb) and *s*(Sb) orbitals. The bonds are somewhat enhanced by pi interaction of the p_x(O) and p_y(O) lone pairs (Mulliken contribution ~90%) with p_x and p_y orbitals of Sb contributing the remainder. This bonding situation results in a total WBI of 1.50, and further in an electron density of 0.17 and a Laplacian of 0.56 at the BCP. This clearly indicates that these bonds are more than single bonds; for comparison, numbers indicating a single bond present in $SbCl_3$ are 1.07 for the WBI, 0.09 for the density and 0.12 for the Laplacian at the BCP. NBO charges amount to −1.14 for the O atoms and to +2.62 for Sb, thus giving an overall charge of +0.34 for the O-Sb-O fragment. NBO charge is −0.84 per OTf unit, suggesting highly polarized character for the equatorial bonds. Consequently, one finds only one localized MO per equatorial bond that has contributions from both Sb and O. It is dominated by the *p*(O) orbital perpendicular to the Sb-O-S plane (85%), the remainder is distributed among the matching *p* orbitals at S and Sb. This yields much lower WBI (0.37), as well as lower numbers for density (0.06) and Laplacian (0.16) at the BCP than for the axial bonds. This is also in line with calculated much longer bond length for the equatorial bonds (2.270 Å), than for the axial bonds (1.829 Å). The latter on the other hand are very similar to those calculated for bare $(OSbO)^+$, 1.784 Å. Overall, the anion can thus be quite reasonably described as an $(OSbO)^+$ unit ionically bonded to four $(OTf)^-$ units.

The calculated Sb1−O1 and Sb2−O1 interatomic distances of the optimized structure of **2** are 1.954 Å and 1.984 Å, respectively, in close agreement with experimental bonding parameters, while the Sb1−O1−Sb2 angle of 123.5° is slightly wider. NBO charges on Sb1 and Sb2 are +1.42 and +2.00, respectively, and −1.29 for the O atom (Table S9). WBO values for Sb1−O1 and Sb2−O1 are 0.57 and 0.50, respectively (Table S8), and involve a set of strong donor-acceptor interactions between O^{2-} and each Sb center (Table S13).

Reactivity

Given the low bond dissociation energy of the Sb−Sb bond in the cation of **1** and rapid transformation of **1** to **2** along with generation of [LSb](OTf), we have compared the reactivity of **1** (Fig. 4) with that of [LSb](OTf)[30]. Compound **1** was prepared in situ for each reactivity study owing to its poor thermal stability. Addition of elemental sulfur to the intense red-colored dichloromethane solution of **1** led to its immediate decolorization, accompanied by Sb(0) precipitation.

https://doi.org/10.1038/s41467-026-70910-5

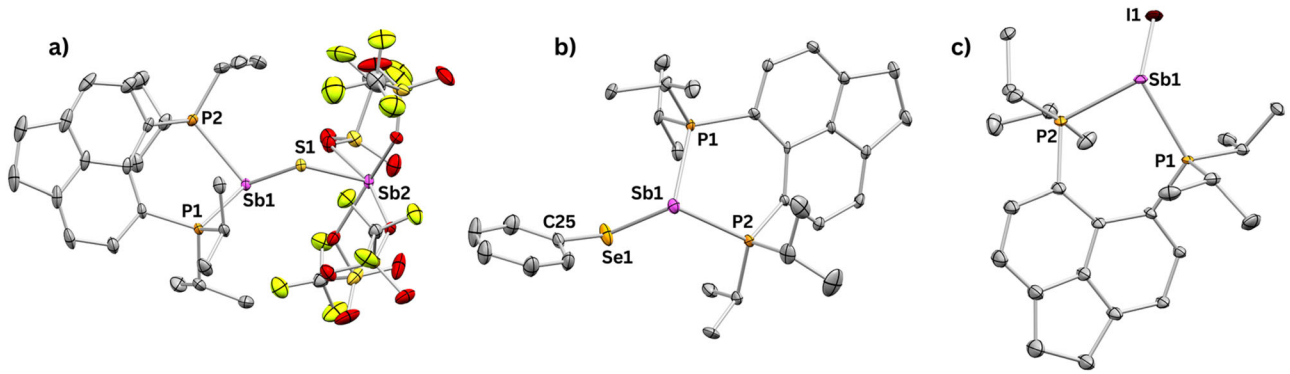

Fig. 5 | ORTEPs of sulphido-bridged diantimony compound 3, the bis(phosphine)-coordinated Sb(III)-SePh dication in compound 6, and the bis(phosphine)-coordinated Sb(III)-I dication in compound 7. a ORTEP of **3** [LSb–S–Sb(OTf)$_4$] in the solid state (thermal ellipsoids at 35%, H atoms, and solvent molecule are omitted for clarity), Selected bond lengths [Å] and angles [°]: P1–Sb1 2.569(2), P2–Sb1 2.577(2), Sb1–S1 2.401(1), Sb2–S1 2.423(1); P1–Sb1–P2 86.64(5), Sb1–S1–Sb2 101.65(5). **b** Molecular structure of the cation in **6** [LSb–SePh]$^{2+}$ in the solid state (thermal ellipsoids at 35%, H atoms, triflate anions, and solvent molecule are omitted for clarity), Selected bond lengths [Å] and angles [°]: P1–Sb1 2.551(2), P2–Sb1 2.572(2), Sb1–Se1 2.5368(9), Se1–C25 1.942(1); P1–Sb1–P2 88.28(6), Sb1–Se1–C25 94.95(2). **c** Molecular structure of the cation in **7** [LSbI]$^{2+}$ in the solid state (thermal ellipsoids at 35%, H atoms, triflate anions, and solvent molecule are omitted for clarity), Selected bond lengths [Å] and angles [°]: P1–Sb1 2.578(2), P2–Sb1 2.587(2), Sb1–I1 2.6972(6); P1–Sb1–P2 85.62(5). The color code refers to the colors used in the crystal structure figures: Sb (magenta), P (orange), O (red), S (yellow), F (light green), Se (light orange), I (dark brown), C (gray).

Colorless single crystals of [LSb–S–Sb(OTf)$_4$] (**3**; Fig. 4a) were obtained in 48% yield by slow diffusion of pentane into the concentrated dichloromethane solution kept at −35 °C. Compound **3** crystallizes in the triclinic space group $P\bar{1}$ (Table S19). The molecular structure of **3** (Fig. 5a) is analogous to that of **2**, having an Sb–S–Sb bridge in place of the Sb–O–Sb unit present in **2**. The Sb–S bond lengths and Sb–S–Sb bond angle match with previously reported Sb–S–Sb compounds[47].

The reaction between [LSb](OTf) and S_8, on the other hand, led to a metathesis reaction forming [LS](OTf)$_2$ (**4**) along with Sb(0) precipitation. Colorless single crystals of **4** were grown in 12% yield at room temperature from dichloromethane/pentane layering. The $^{31}P\{^1H\}$ NMR spectrum of **4** in CD_3CN shows a signal at +64 ppm (Figure S46). An in-situ NMR study shows the formation of L(OTf)$_2$ and numerous P(V) species in the reaction (Figure S49). Compound **4** crystallizes in the triclinic space group $P\bar{1}$ (Table S19) exhibiting P1–S1 and P2–S1 bond lengths of 2.092(1) and 2.086(1), respectively, and has a P1–S1–P2 bond angle of 103.91(5)° (Figure S48).

Reactions of **1** with diphenyl dichalcogenides (Ph_2Ch_2, Ch = S, Se) led to pale-yellow-colored solutions along with the precipitation of Sb(0) (Fig. 4b). Single crystals of [LSb-ChPh](OTf)$_2$ (Ch = S (**5**) and Se (**6**)) were obtained in good yields from respective dichloromethane solutions upon layering with pentane and kept at low temperature. Both **5** and **6** crystallize in the triclinic space group $P\bar{1}$ (Table S20). The Sb1 sites have a trigonal pyramidal environment, with Sb1–S1 and Sb1–Se1 bond lengths being 2.399(2) and 2.5368(9) Å in **5** and **6**, respectively (Figs. S54, 5b). These Sb–Ch bond lengths are shorter than those in the reported neutral chalcogen-stibine complexes[48,49]. The $^{31}P\{^1H\}$ NMR spectra in CD_3CN show peaks at +16.6 and +11.6 ppm for **5** and **6**, respectively (Figure S52 and S59). Solid-state absorbance spectra for **5** and **6** show λ_{max} at 315 nm and 310 nm, respectively (Figure S55 and S62). On the contrary, an in-situ $^{31}P\{^1H\}$ and ^{77}Se NMR study (Figure S56, S63 and S64) upon addition of diphenyl dichalcogenide to [LSb](OTf) shows that the Ch–Ch bond was not cleaved. However, elemental Sb precipitated from the reaction medium with the corresponding formation of L(OTf)$_2$ (Figure S63 and S64). This observation suggests that the difference in local charges between the Sb centers in the cation in **1** stimulates the Ch–Ch bond cleavage[50].

Recently, we have reported a metathesis reaction upon treatment of [LSb](OTf) with triiodophosphane, giving [LP](OTf)[51]. A similar metathesis reaction was not observed upon combining **1** with triiodophosphane. Pale yellow single crystals of [LSbI](OTf)$_2$ (**7**) (Fig. 4c) were isolated in 45% yield from a dichloromethane solution layered with pentane stored at a low temperature. The $^{31}P\{^1H\}$ NMR spectrum of **7** in CD_3CN depicts a peak at +4.97 ppm (Figure S67). The solid-state absorbance spectrum of **7** shows λ_{max} at 307 nm (Figure S69). Compound **7** crystallizes in the monoclinic space group *C*2/*c* (Table S20). The Sb atom in the cationic molecule in **7** possesses a trigonal pyramidal environment (Fig. 5c). The Sb–I bond length is 2.6971(6) Å, which is slightly longer than that reported for free SbI_3 (2.686(1) Å)[52] but shorter than that present in polymeric pyridine-based antimony(III) iodides (Sb–I = 2.7878(5) Å)[52]. The role of PI_3 as an iodine source is apparent for the formation of **7**[53].

A unique Sb-Co compound [(LSb)$_3$Co$_3$(CO)$_9$SbCl][SbF$_6$]$_4$ (**8**) was obtained from the reaction between **1** and [$Co_2(CO)_8$] followed by anion exchange with Ag[SbF$_6$] (Fig. 6a). Black crystals of **8** were grown at low temperature from dichloromethane upon layering with pentane. The highly symmetric compound **8** crystallizes in the non-centrosymmetric trigonal space group *R*3*c*, with one-third of the cationic unit and approximately 1.3 [SbF$_6$]$^-$ anions present in the asymmetric unit (Table S20). The central antimony atom, Sb2, and one of the [SbF$_6$]$^-$ units are located on a three-fold rotational axis within the asymmetric unit, while the other [SbF$_6$]$^-$ anion resides on a general position. The molecular structure of **8** (Fig. 6b) shows Sb2 in a distorted tetrahedral coordination environment. The Sb2–Cl1 bond length falls in the range of that observed in cyclic-alkyl-amino-carbene-stabilized chloro-stibinidenes[54]. The Sb1–Co1 and Co1–Sb2 bond lengths (2.528(3) Å and 2.521(3) Å respectively) in **8** are nearly the same, being marginally smaller than those in distibinidene-coordinated [Co(CO)$_4$][55], a bis(α-iminopyridine)-stabilized [Sb-Co(CO)$_3$-Sb] complex[22] or a stibinidene-stabilized [Co(CO)$_3$] complex reported by Zhou and co-workers[56], and also the related distibine-cobalt complexes reported by Bismuto and co-workers[57,58]. Notably, the average Sb–Co bond lengths (2.596 Å) found in the structurally related cation [Sb{Co(CO)$_3$PPh$_3$}$_4$]$^+$ is longer than that in **8**[59]. A relatable homoleptic complex is [Sb(AuMe)$_4$]$^{3-}$, with an Sb atom in a tetrahedral coordination environment[60]. CO vibrational frequencies arising from the {Co(CO)$_3$} fragments in **8** appear at 1972, 2022, and 2094 cm^{-1}, as determined by IR spectroscopy (Figure S76), which is comparable to the reported stibinidene- and distibine-cobalt carbonyl complexes[22,55–57].

Whitmire et al. reported a structurally analogous complex, (Et$_4$N)$_2$[ClSbFe$_3$(CO)$_{12}$][61], obtained from the treatment of (Et$_4$N)$_3$[SbFe$_4$(CO)$_{16}$] with $SbCl_3$ or $TlCl_3$. In our case, dichloromethane served as the chloride source for the formation of **8**. Compound **8** was characterized by NMR spectroscopy in the solution

https://doi.org/10.1038/s41467-026-70910-5

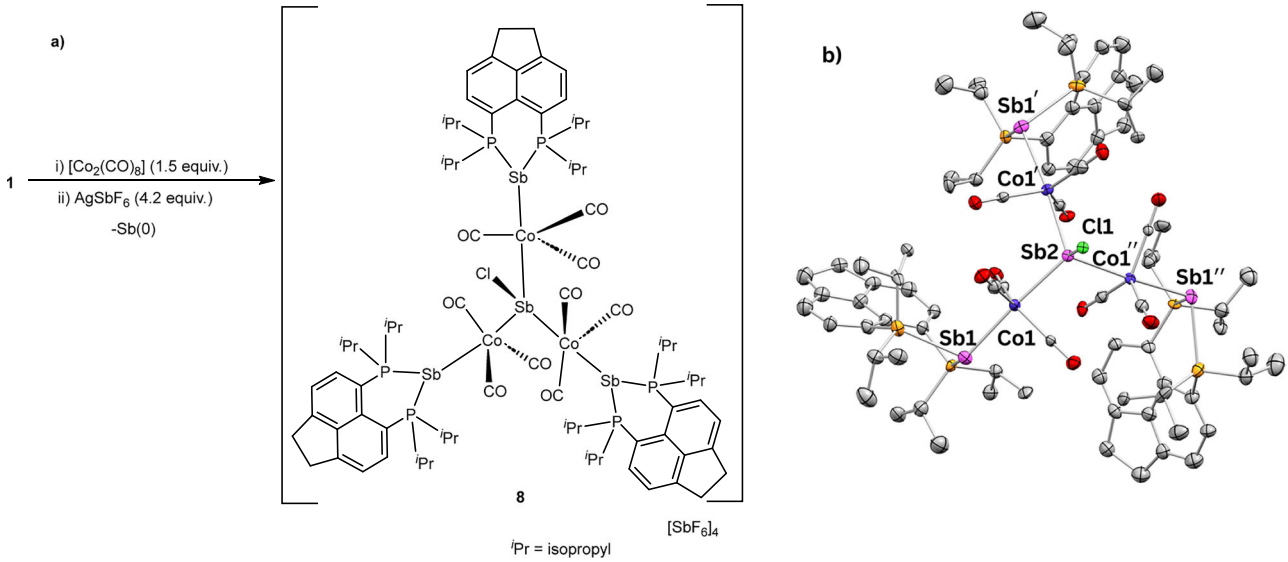

Fig. 6 | Reaction scheme of 1 with [Co2(CO)8] forming 8, and molecular structure determination. a Reaction of **1** with 1.5 equivalents of $[Co_2(CO)_8]$ in dichloromethane, followed by anion exchange using $Ag[SbF_6]$. (Note: $L(OTf)_2$ and phosphine oxides were detected by a $^{31}P\{^1H\}$ in-situ NMR study of the reaction) (**b**) Molecular structure of the cation in **8** $[(LSb)_3Co_3(CO)_9SbCl]^{4+}$ in the solid state (thermal ellipsoids at 35%, H atoms, $[SbF_6]^-$ anions, and solvent molecule are omitted for clarity). Selected bond lengths [Å] and angles [°]: Sb1–Co1 2.528(3), Sb2–Co1 2.521(3), Sb2–Cl1 2.441(7); Co1–Sb2–Cl1 104.39(6). The color code refers to the colors used in the crystal structure figures: Sb (magenta), P (orange), O (red), Co (blue), Cl (green), C (gray).

state (Figure S70–S73) and exhibited diamagnetic behavior in the temperature range 50–300 K (Figure S78–S80). The optimized structure of **8** agreed with the structural parameters obtained from the single crystal X-ray diffraction data (calculated cartesian coordinates are provided in the Source Data file). The lowest excited triplet state is much higher in energy (39 kcal mol^{-1}), coherent with its diamagnetic behavior. A related complex, in $[Cp_2Co][Bi\{Co(CO)_4\}_4]$, was however reported to possess two unpaired electrons[62]. Absorbance data of **8** in dichloromethane reveals a maximal absorption (λ_{max}) at 565 nm ($\varepsilon = 8486\ M^{-1}\ cm^{-1}$) (Figure S74–S75). The spectrum is well reproduced by the TDDFT calculations, albeit somewhat blue-shifted by ~60 nm or 0.26 eV (Table S14). The absorption at λ_{max} is due to two near-degenerate excitations from near-degenerate occupied MOs (representations in idealized threefold symmetry) to the (non-degenerate) LUMO. Also, the subsequent two pairs of excitations are near-degenerate and show similar character (Table S14). The localized molecular orbitals (LMOs) (Table S15) reveals that the central Sb atom is covalently bonded to the three Co atoms and exhibits one strongly polarized bond to Cl. Each of the three peripheral Sb atoms bind to the two neighbored P atoms (polarized towards P), further covalently bonds to one Co atom and additionally have one lone pair of electrons on it. For each Co atom, seven further LMOs involve the Co(*d*) and the C(*p*) orbitals of the three binding CO groups. Three of them represent σ-type interactions with main localization at C, four of them are dominantly located at Co with substantial π-type delocalization towards C. We note in passing that the local bond situation at Co is reasonably well-resembled in the simple model compound $[H\text{-}Co(CO)_3\text{-}H]^-$, for which the analogous LMOs are also shown in Table S15. No Sb-Co complex could be crystallized from the reaction between [LSb](OTf) and $[Co_2(CO)_8]$.

Hence, a disparate reactivity profile of **1** and [LSb](OTf) is evident from the above discussed experimental findings. The observed reactivity of **1** is guided by the presence of the highly reactive counter-trianion as well as the polarity and the low dissociation energy of the Sb–Sb bond. Furthermore, the redox non-innocence of bis(phosphine) leads to multiple redox processes. Unlike the reported examples of $\{Pn_3\}$-based monocationic units acting as a "Pn" transfer reagent[25,26], **1** did not act as a synthon for the transfer of the central "Sb" to create other low-valent organoantimony compounds, and it did not undergo coordination to other metal ions or Lewis acids.

In summary, we showcase the hitherto unknown acyclic triantimony-based tricationic species as the latest innovation in the synthetic toolbox of multiply charged ions. Structural and electronic delineation of the tricationic part shows an overall W-shaped molecular conformation comprising a low-valent $\{Sb_3\}$ unit terminally capped by bis(phosphine)s. The $\{Sb_3\}$ unit features a foundationally weak three-center four-electron σ-bonding between the atoms, with the central Sb atom possessing two lone pairs of electrons. The unconventional $[Sb(O)_2(OTf)_4]^{3-}$ counter trianion shows the presence of highly reactive polar $Sb^{\delta+}\text{–}O^{\delta-}$ bonds. This triantimony-based compound **1** is thermally unstable and appears as a fleeting species before it converts to the diantimony oxo compound **2**. Compound **1** exhibits a diverse reactivity, which arises not only from the $Sb^{\delta+}\text{–}O^{\delta-}$ bond polarity in the counter trianion, but also from a weak Sb–Sb σ-bond and the bond polarity in the trication of the compound. In summary, we have been able to chemically realize an acyclic trantimony-based tricationic species, enriching the landscape of antimony chemistry. We will continue our investigations in the preparation of such exotic multiply-charged cationic species that will introduce new bonding schemes and novel reactivity.

Methods

General methods

All manipulations were carried out under a protective argon atmosphere, applying standard Schlenk techniques or in a dry box. Dichloromethane (DCM) was stirred, refluxed over calcium hydride, and kept over 3 Å molecular sieves. All solvents were distilled and stored under argon, and degassed before use. CD_3CN and CD_2Cl_2 ampoules were purchased from Sigma Aldrich and are used as they are. [LSb](OTf) and $Sb(OTf)_3$ (OTf = CF_3SO_3) were made following the literature procedures[16,28]. All chemicals were used as purchased.

Spectroscopic details (NMR, IR, UV-Vis, ESI-MS, and MALDI-TOF)

^1H and $^{13}C\{^1H\}$ NMR spectra were referenced to external $SiMe_4$ using the residual signals of the deuterated solvent (^1H) or the solvent itself (^{13}C). $^{19}F\{^1H\}$, $^{31}P\{^1H\}$ and $^{77}Se\{^1H\}$ NMR were referenced to external $C_6H_5CF_3$

(TFT), 85% H_3PO_4, and $SeMe_2$ (plus 5 % C_6D_6) respectively. NMR spectra were recorded on Bruker AVANCE III HD ASCEND 9.4 Tesla/400 MHz, Jeol 9.4 Tesla/400 MHz, and Bruker AVANCE III HD ASCEND 14.1 Tesla/600 MHz. Solution and solid phase absorbance spectra were acquired from SHIMADZU UV-1900 and UV-3600 plus UV-VIS-NIR spectrophotometer using quartz cells with a path length of 1 cm. Melting points were determined under argon in closed NMR tubes and were uncorrected. Due to the high sensitivity of the compounds, Elemental analyses did not provide consistent data. Mass analysis was performed in MALDI-TOF Applied Biosystems − 4800 Plus MALDI TOF/TOF Analyzer and in AB Sciex 4800 plus HRMS on the Waters Synapt, USA. Infrared spectroscopic data were recorded in Bruker Alpha-II FTIR-Eco ATR and Opus software. All spectroscopic data plots are given in the Supplementary Information.

Syntheses

Synthesis of compound 1. Three equivalents of [LSb](OTf) (0.050 g, 0.077 mmol) and one equivalent of $Sb(OTf)_3$ (0.014 g, 0.025 mmol) were added to a Schlenk flask, and 4 mL DCM (pre-cooled at −35 °C) was added to it. The reaction mixture was stirred for 15 minutes at −35 °C. A dark red-colored solution was obtained. The solution was stored at −35 °C for one day. Red-colored crystals were obtained. A scale-up of the crystallization yield of **1** was possible using dichloroethane as the solvent. The crystals were thermally sensitive in addition to being extremely air- and moisture-sensitive. λ_{max} (acetonitrile) = 418 nm ($\varepsilon = 1030.83\ M^{-1}\ cm^{-1}$).

^{1}H NMR (600 MHz, CD_3CN, 243 K) δ 8.09 (d, $^3J_{HH}$ = 7.4 Hz, 2H, Acn-C*H*), 7.67 (d, $^3J_{HH}$ = 7.4 Hz, 2H, Acn-C*H*), 3.54 (s, 4H, Acn-CH_2), 2.79 (m, 4H, ^{i}Pr-C*H*), 1.08 (m, 24H, ^{i}Pr-CH_3) ppm.

^{31}P{^{1}H} NMR (162 MHz, CD_3CN, 243 K) δ +17.19 ppm.

^{19}F{^{1}H} NMR (565 MHz, CD_3CN, 243 K) δ −80.09 ppm.

^{13}C{^{1}H} NMR was not possible due to the high instability of the compound.

% Yield calculated for compound **1** from ^{31}P{^{1}H} in-situ reaction NMR spectra using triphenyl phosphate as the internal standard = 15

Synthesis of compound 2. Three equivalents of [LSb](OTf) (0.050 g, 0.077 mmol) and one equivalent of $Sb(OTf)_3$ (0.014 g, 0.025 mmol) were added to a Schlenk flask, and 8 mL DCM was added to it. The reaction mixture was stirred for 24 hours at room temperature. A light orange solution was obtained along with the formation of Sb(0). The solution was filtered, layered with pentane, and kept for crystallization at −35 °C. White-colored single crystals were obtained after 2 days in 38% (0.036 g) yield. Decomposition temperature: 148-150 °C. MALDI-TOF (CHCA Matrix) found m/z 343.4080, calculated for $[C_{24}H_{36}P_2Sb_2OK]^{4+}$ m/z 343.4976.

^{1}H NMR (600 MHz, CD_3CN, 298 K) δ 8.11 (d, $^3J_{PH}$ = 15.3 Hz, 2H, Acn-C*H*), 7.70 (d, $^3J_{HH}$ = 7.6 Hz, 2H, Acn-C*H*), 3.56 (s, 4H, Acn-CH_2), 2.87 (m, 4H, ^{i}Pr-C*H*), 1.19 (m, 12H, ^{i}Pr-CH_3), 1.04 (m, 12H, ^{i}Pr-CH_3) ppm.

^{13}C{^{1}H} NMR (151 MHz, CD_3CN, 298 K) δ 161.02 (s, Acn-*C*), 142.82 (d, *J* = 8.3 Hz, Acn-*C*), 142.32 (m, Acn-*C*), 135.90 (m, Acn-*C*), 123.14 (m, Acn-*C*H), 122.17 (q, *J* = 321.6 Hz, OTf) 103.08, 102.60 (s, Acn-*C*H), 31.47 (s, Acn-*C*H_2), 23.27 (d, *J* = 42.8 Hz, ^{i}Pr-*C*H), 17.31 (s, ^{i}Pr-*C*H_3), 16.46 (s, ^{i}Pr-*C*H_3), ppm.

^{31}P{^{1}H} NMR (162 MHz, CD_3CN, 298 K) δ +17.77 ppm.

^{19}F{^{1}H} NMR (565 MHz, CD_3CN, 298 K) δ −79.20 ppm.

Single-crystal X-ray diffraction

Single crystal data were collected on Bruker SMART APEX Duo and Bruker APEX-II CCD diffractometers using Mo radiation (0.71073 Å). The structures were solved using SHELXT methods from SHELXL-2018/136 and refined using full-matrix least-squares methods against F2 with the SHELXL program. Olex2 was used as a graphical interface for the refinements. General crystallographic data are listed in Supplementary Tables S12 and S13; Structural images are shown in Fig. 2b–d, Fig. 5a–c, Fig. 6b; supplementary structural images are shown in Supplementary Figs. S22& S28.

SQUID measurements

The samples were characterized using a SQUID-Vibrating Sample Magnetometer (SQUID-VSM, Quantum Design, USA) to determine their magnetic behavior. The magnetization of the sample was recorded as a function of temperature in the range of 5-300 K, under: a) Magnetic field of 1000 Oe; b) Zero field-cooled (ZFC) and field-cooled (FC) conditions. The sample was cooled in zero fields to 5 K for ZFC measurements, and then magnetization was measured while warming in a field of 1000 Oe. For FC measurement, the sample was cooled from 300 K to 5 K in a magnetic field of 1000 Oe, and the magnetization was measured while warming in a field. Magnetization versus magnetic field (M-H) at 300 K, 6 K, 5 K, and 4 K up to a magnetic field of 1000 Oe was done. Prior to the measurement, the instrument was calibrated using a standard sample of high-purity Palladium metal at 298 K and 1 Tesla magnetic field in VSM mode. During the calibration, it was ensured that the experimentally obtained magnetization of the Pd sample (in VSM mode) matches closely with its theoretical value. During calibration, the obtained error was less than 0.2%.

Quantum chemical studies

For the cation in compound **1** and for compound **2**, gas-phase geometry optimizations were carried out using program packages ORCA 5.0.1[42] starting from the corresponding X-ray crystallographic structures. The optimizations were performed at the BP86[63,64]-D4[65]/def2-TZVPP[66] level of theory. The RI-J approximation was applied for Coulomb integrals with the appropriate auxiliary basis sets[67]. Each optimized geometry was confirmed as a minimum by evaluating its Hessian matrix. Natural Bond Orbital (NBO)[68] analyses were done with Gaussian 16 Rev. B.01 software[69]. The NBO results provided insights into selected orbital interactions, partial atomic charges, donor–acceptor interactions, and Wiberg Bond Orders (WBOs)[70]. Molecular Electrostatic Potential (MEP) maps were generated to visualize electron-rich and electron-deficient regions of the molecules. Topological analyses, including Atoms-in-Molecules (AIM) charge distribution and Non-Covalent Interaction (NCI) plots, were carried out using the Multiwfn 3.8 software[71]. Figures were rendered by Gaussview 5.0 package program [72].

Analogous calculations with the same settings were done for the anion in **1** and for compound **8** with TURBOMOLE[44], the clarification of the bond situation was done via localized molecular orbitals[46]. Further, with the same program suite, time-dependent density functional calculations for the cation in **1** and for compound **8** were done employing the PBE0[73] functional (all other settings unchanged).

Data availability

The structure of compounds **1**–**8** were determined by single-crystal X-ray diffraction. Crystallographic data for the structures reported in this article have been deposited at the Cambridge Crystallographic Data Center, under deposition numbers CCDC-2475487-2475489 (**1**–**3**), 2475493-2475496 (**4**–**7**), 2475624 (**8**). A copy of the data can be obtained free of charge via (https://www.ccdc.cam.ac.uk/structures/). The Cartesian coordinates of all optimized structures are provided in the source data file. The files comprise all necessary data for reproducing the values. All non-default parameters for the computational studies are given in the Supplementary Information together with the corresponding references of the used methods. The data collected for NMR, UV-Vis, mass spectrometry, SQUID and EPR measurements and the respective discussions are provided in the supplementary data file. All data are available from the corresponding author upon request. Source data are provided with this paper.

Code availability

The ORCA quantum chemical program package is available at (https://orcaforum.kofo.mpg.de/app.php/dlext/), and TURBOMOLE at (https://www.turbomole.org/).

References

1. Melen, R. L. Frontiers in molecular p-block chemistry: from structure to reactivity. *Science* **363**, 479–484 (2019).
2. Power, P. P. Main-group elements as transition metals. *Nature* **463**, 171–177 (2010).
3. Böhme, D. K. Multiply-charged ions and interstellar chemistry. *Phys. Chem. Chem. Phys.* **13**, 18253–18263 (2011).
4. Pauling, L. The normal state of the helium molecule-ions He_2^+ and He_2^{++}. *J. Chem. Phys.* **1**, 56–59 (1933).
5. Schröder, D. & Schwarz, H. Generation, stability, and reactivity of small, multiply charged ions in the gas phase. *J. Phys. Chem. A* **103**, 7385–7394 (1999).
6. Schröder, D. Coulombic explosions and stability of multiply charged ions in the gas phase. *Angew. Chem. Int. Ed.* **43**, 1329–1331 (2004).
7. Boldyrev, A. I., Gutowski, M. & Simons, J. Small multiply charged anions as building blocks in chemistry. *Acc. Chem. Res.* **29**, 497–502 (1996).
8. Wilson, R. J., Lichtenberger, N., Weinert, B. & Dehnen, S. Intermetalloid and heterometallic clusters combining p-block (semi) metals with d- or f-block metals. *Chem. Rev.* **119**, 8506–8554 (2019).
9. Barthélemy, A. & Krossing, I. Cationic group 13 and 14 element clusters. *Inorg. Chem.* **63**, 21763–21787 (2024).
10. Back, O., Donnadieu, B., Parameswaran, P., Frenking, G. & Bertrand, G. Isolation of crystalline carbene-stabilized P_2-radical cations and P_2-dications. *Nat. Chem.* **2**, 369–373 (2010).
11. Abraham, M. Y. et al. Oxidation of carbene-stabilized diarsenic: diarsene dications and diarsenic radical cations. *J. Am. Chem. Soc.* **135**, 2486–2488 (2013).
12. Ho, L. P. et al. London dispersion interactions in pnictogen cations $[ECl_2]^+$ and $[E{=}E]^{2+}$ (E=P, As, Sb) supported by anionic *N*-heterocyclic carbenes. *Chem. Eur. J.* **24**, 18922–18932 (2018).
13. Weinert, H. M. et al. Metal-coordinated distibene and dibismuthene dications – isoelectronic analogues of butadiene dications. *Chem. Commun.* **59**, 7755–7758 (2023).
14. Dabringhaus, P., Molino, A. & Gilliard, R. J. Carbodiphosphorane-activated distibene and dibismuthene dications. *J. Am. Chem. Soc.* **146**, 27186–27195 (2024).
15. Béland, V. A., Nöthling, N., Leutzsch, M. & Cornella, J. Activation and catalytic degradation of SF6 and PhSF5 at a bismuth center. *J. Am. Chem. Soc.* **146**, 25409–25415 (2024).
16. Fernando, S. et al. Zwitterionic heavier pnictinidenes in redox catalysis. *Angew. Chem. Int. Ed.* **64**, e202505697 (2025).
17. Chitnis, S. C., Burford, N., Weigand, J. J. & McDonald, R. Reductive catenation of phosphine antimony complexes. *Angew. Chem. Int. Ed.* **54**, 7828–7832 (2015).
18. Chitnis et al. Synthesis and reactivity of cyclotetra(stibinophosphonium) tetracations: redox and coordination chemistry of phosphine–antimony complexes. *Chem. Sci.* **6**, 2559–2574 (2015).
19. Schwedtmann, K. et al. Formation of an imidazoliumyl-substituted $[(L_C)_4P_4]^{4+}$ tetracation and transition metal mediated fragmentation and insertion reaction (L_C = NHC). *Chem. Sci.* **10**, 6868–6875 (2019).
20. Yadav, R. et al. Supramolecular trapping of a cationic all-metal σ-aromatic $\{Bi_4\}$ ring. *Nat. Chem.* **16**, 1523–1530 (2024).
21. Glootz, K. et al. Tetracationic gallium cluster cations. *Angew. Chem. Int. Ed.* **57**, 14203–14206 (2018).
22. Haldar, H. et al. Tetra-Cationic distibane stabilized by Bis(α-iminopyridine) and Its reactivity. *J. Am. Chem. Soc.* **147**, 3140–3151 (2025).
23. Back, J. et al. Triazenyl radicals stabilized by N-heterocyclic carbenes. *J. Am. Chem. Soc.* **139**, 15300–15303 (2017).
24. Holthausen, M. H., Surmiak, S. K., Jerabek, P., Frenking, G. & Weigand, J. J. [3+2] fragmentation of an $[RP_5Cl]^+$ cage cation induced by an *N*-heterocyclic carbene. *Angew. Chem. Int. Ed.* **52**, 11078–11082 (2013).
25. Tondreau, A. M., Benkö, Z., Harmer, J. R. & Grützmacher, H. Sodium phosphaethynolate, Na(OCP), as a "P" transfer reagent for the synthesis of N-heterocyclic carbene supported P3 and PAsP radicals. *Chem. Sci.* **5**, 1545–1554 (2014).
26. Spinnato, D. et al. A trimetallic bismuth(I)-based allyl cation. *Nat. Chem.* **17**, 265–270 (2025).
27. Neumann, N. et al. Fragmentation dynamics of CO_2^{3+} investigated by multiple electron capture in collisions with slow highly charged ions. *Phys. Rev. Lett.* **104**, 10321 (2010).
28. Ma, C. et al. Three-body fragmentation dynamics of $CH_2CCH_2^{3+}$ investigated by 50-keV/u Ne^{8+} impact. *Phys. Rev. A* **101**, 052701 (2020).
29. He, Z. et al. Sequential deprotonation of the allene trication produced by 30-keV/u He^{2+} impact. *Phys. Rev. A* **105**, 022818 (2022).
30. Kumar, V., Gonnade, R. G., Yildiz, C. B. & Majumdar, M. Stabilization of the elusive antimony(I) cation and its coordination complexes with transition metals. *Angew. Chem. Int. Ed.* **60**, 25522–25529 (2021).
31. Bondi, A. van der Waals volumes and radii. *J. Phys. Chem. A* **68**, 441–451 (1964).
32. Bartlett, R. A. et al. Isolation and structural characterization of the solvated lithium salts of the main group 5 anions $[EPh_2]^-$(E = N,P, As, or Sb) and $[Sb_3Ph_4]^-$. *J. Am. Chem. Soc.* **108**, 6921–6926 (1986).
33. Althaus, H., Breunig, H. J., Probst, J., Rösler, R. & Lork, E. The crystal structure of a trinuclear anion, $[(t\text{-}Bu_2Sb)_2Sb]^-$ formed by reaction of cyclo-(t-Bu_4Sb_4) with potassium, and the four-membered rings, cyclo-(t-$Bu_4E_nSb_{4-n}$) (E = P, n = 0-3; E = As, n = 0-2). *J. Organomet. Chem.* **585**, 285–289 (1999).
34. Howatson, J., Grev, D. M. & Morosin, B. Crystal and molecular structure of uranyl acetate dihydrate. *J. Inorg. Nucl. Chem.* **37**, 1933–1935 (1975).
35. Wenger, J. S., Weng, M., George, G. N. & Johnstone, T. C. Isolation, bonding and reactivity of a monomeric stibine oxide. *Nat. Chem.* **15**, 633–640 (2023).
36. Kather, R. et al. Lewis-acid induced disaggregation of dimeric arylantimony oxides. *Chem. Commun.* **51**, 5932–5935 (2015).
37. Kuziola, J. et al. Synthesis and characterization of monomeric triarylbismuthine oxide. *Angew. Chem. Int. Ed.* **64**, e202415169 (2025).
38. Bordner, J., Doak, G. O. & Everett, T. S. Crystal Structure of 2,2,4,4,-tetrahydro-2,2,4,4,-hexaphenyl-1,3,2,4-dioxadistibetane (Triphenylstibine Oxide Dimer) and related compounds. *J. Am. Chem. Soc.* **108**, 4206–4213 (1986).
39. Chen, C.-H. & Gabbaï, F. P. Coordination of a stibine oxide to a Lewis acidic stiborane at the upper rim of the biphenylene backbone. *Dalton Trans.* **47**, 12075–12078 (2018).
40. Chitnis, S. S., Robertson, A. P. M., Burford, N., Patrick, B. O., McDonald, R. & Ferguson, M. J. Bipyridine complexes of E^{3+} (E = P, As, Sb, Bi): strong Lewis acids, sources of $E(OTf)_3$ and synthons for E^{I} and E^{V} cations. *Chem. Sci.* **6**, 6545–6555 (2015).
41. Chitnis, S. S., Vos, K. A., Burford, N., McDonald, R. & Ferguson, M. J. Distinction between coordination and phosphineligand oxidation: interactions of di- and triphosphines with Pn^{3+} (Pn = P, As, Sb, Bi). *Chem. Commun.* **52**, 685–688 (2016).
42. Neese, F. Software update: the ORCA program system, Version 5.0. *WIREs Comput. Mol. Sci.* **12**, e1606 (2022).
43. Scharf, L. T., Andrada, D. M., Frenking, G. & Gessner, V. H. The bonding situation in metalated ylides. *Chem. Eur. J.* **23**, 4422–4434 (2017).
44. TURBOMOLE Version 7.9, TURBOMOLE GmbH 2024. TURBOMOLE is a development of University of Karlsruhe and Forschungszentrum Karlsruhe 1989–2007, TURBOMOLE GmbH since 2007 https://www.turbomole.org (2007).

45. Pausch, A. Consistent analytical second derivatives of the Kohn–Sham DFT energy in the framework of the conductor-like screening model through Gaussian charge distributions. *J. Chem. Theory Comput.* **20**, 3169–3183 (2024).
46. Pipek, J. & Mezey, P. G. A fast intrinsic localization procedure applicable for ab initio and semiempirical linear combination of atomic orbital wave functions. *J. Chem. Phys.* **90**, 4916–4926 (1989).
47. Jia, D.-X., Zhang, Y., Dai, J., Zhu, Q.-Y. & Gu, X.-M. Solvothermal synthesis and crystal structure of Sb(III) and Sb(V) thioantimonates: $[Mn(en)_3]Sb_2S_5$ and $[Ni(en)_3(Hen)]SbS_4$. *J. Solid State Chem.* **177**, 2477–2483 (2004).
48. Le, L. et al. Base-promoted reactions of organostibines with alkynes and organic halides to give chalcogenated (Z)-olefins and ethers. *Org. Lett.* **24**, 6159–6164 (2022).
49. Ganesamoorthy, C., Wölper, C., Dostál, L. & Schulz, S. Syntheses and structures of N,C,N-stabilized antimony chalcogenides. *J. Org. Chem.* **845**, 38–43 (2017).
50. Inés, B., Holle, S., Goddard, R. & Alcarazo, M. Heterolytic S-S bond cleavage by a purely carbogenic frustrated lewis pair. *Angew. Chem. Int. Ed.* **49**, 8389–8391 (2010).
51. Mukherjee, N., Kumar, V., Yildiz, C. B. & Majumdar, M. Reactivity study of the bis(phosphine)-stabilized antimony(i) cation. *Inorg. Chem.* **63**, 24306–24312 (2024).
52. Pomogaeva, A. V., Khoroshilova, O. V., Davydova, E. I., Suslonov, V. V. & Timoshkin, A. Y. Antimony(III) Iodide Complexes with Pyridine: Structures and bonding via three pnictogen bonds. *Z. Anorg. Allg. Chem.* **647**, 687–695 (2021).
53. Ellis, B. D., Dyker, C. A., Decken, A. & McDonald, C. L. B. The synthesis, characterization and electronic structure of N-heterocyclic carbene adducts of P^{I} cations. *Chem. Commun.* **21**, 1965–1967 (2005).
54. Kretschmer, R., Ruiz, D. A., Moore, C. E., Rheingold, A. L. & Bertrand, G. One-, two-, and three-electron reduction of a cyclic alkyl-(amino) carbene–$SbCl_3$ adduct. *Angew. Chem. Int. Ed.* **53**, 8176–8179 (2014).
55. Vránová, I. et al. Stibinidene and bismuthinidene as two-electron donors for transition metals (Co and Mn). *Chem. Eur. J.* **22**, 7376–7380 (2016).
56. Zhang, L., Huang, M. & Zhou, J. A dicationic distibine stabilized by intramolecular π–π interaction and second-sphere coordination. *Chem. Commun.* **61**, 8592–8595 (2025).
57. Meleschko, D. et al. Light-dependent reactivity of heavy pnictogen double bonds. *Angew. Chem. Int. Ed.* **63**, e202405400 (2024).
58. Meleschko, D. et al. Synthesis, reactivity, and theoretical insights of Co-Sb_2 and Co-Bi_2 rings. *Organometallics* **43**, 2581–2588 (2024).
59. Cobbledick, R. E. & Einstein, F. W. B. The crystal structure of μ4-antimonio-tetrakis[tricarbonyl(triphenylphosphine)cobalt] tetraphenylborate-dichloromethane. *Acta Cryst.* **35**, 2041–2044 (1979).
60. Pan, F., Lukanowski, M., Weigend, F. & Dehnen, S. Tetrahedral $[Sb(AuMe)_4]^{3-}$ occurring in multimetallic cluster syntheses: about the structure-directing role of methyl groups. *Angew. Chem. Int. Ed.* **60**, 25042–25047 (2021).
61. Luo, S. & Whitmire, K. H. Synthesis and characterization of a series of antimony-containing iron carbonyl complexes. *Inorg. Chem.* **28**, 1424–1431 (1989).
62. Leigh, J. S. & Whitmire, K. H. $[Cp_2Co][Bi\{Co(CO)_4\}_4]$: a paramagnetic, ten-electron, tetrahedral complex of bismuth. *Angew. Chem. Int. Ed.* **27**, 396–397 (1988).
63. Perdew, J. P. Density-functional approximation for the correlation energy of the inhomogeneous electron gas. *Phys. Rev. B* **33**, 8822–8824 (1986).
64. Caldeweyher, E. et al. A generally applicable atomic-charge dependent London dispersion correction. *J. Chem. Phys.* **150**, 154122 (2019).
65. Weigend, F. & Ahlrichs, R. Balanced basis sets of split valence, triple zeta valence and quadruple zeta valence quality for H to Rn: Design and assessment of accuracy. *Phys. Chem. Chem. Phys.* **7**, 3297–3305 (2005).
66. Weigend, F. Accurate coulomb-fitting basis sets for H to Rn. *Phys. Chem. Chem. Phys.* **8**, 1057–1065 (2006).
67. Perdew, J. P., Ernzerhof, M. & Burke, K. Rationale for mixing exact exchange with density functional approximations. *J. Chem. Phys.* **105**, 9982–9985 (1996).
68. Gaussian 16, Revision B.01, Frisch, M. J. et al. Gaussian, Inc., Wallingford, CT. (2016).
69. Wiberg, K. B. Application of the pople-santry-segal CNDO method to the cyclopropylcarbinyl and cyclobutyl cation and to bicyclobutane. *Tetrahedron* **24**, 1083–1096 (1968).
70. Lu, T. & Chen, F. Multiwfn: A multifunctional wavefunction analyser. *J. Comput. Chem.* **33**, 580–592 (2012).
71. Nielsen, A.B. & Holder, A.J. Gauss View 5.0, User's Reference. GAUSSIAN Inc., Pittsburgh. (2009).
72. Becke, A.D. et al. Density-functional exchange-energy approximation with correct asymptotic behavior. Phys. Rev. A **38**, 3098–3100 (1988).
73. NBO Version 3.1, Glendening, E.D., Reed, A.E., Carpenter, J.E. & Weinhold, F.

Acknowledgements

MM thanks SERB India SPF/2022/000046, CRG/2022/000673 and Alexander von Humboldt Foundation-Experienced Researchers Program for their support. We thank Prof. Dr. Biprajit Sarkar, Free University Berlin, Germany for recording the EPR spectra for compound 8 using a Bruker EMX instrument connected to an Oxford crysostat for low temperature measurements. We thank Dr. P. R. Rajamohanan, Central NMR Facility, National Chemical Laboratory, Pune for valuable inputs in NMR analysis.

Author contributions

N.M. conceived and performed the synthetic experiments, collected single-crystal X-ray crystallographic data, solved and refined the structures, and prepared samples for further analyses. V.K. has synthesized compound **4**. M.M. has conceptualized and supervised the work. M.P.S. and K.S. performed the SQUID experiments and analysed the data. H.T.A.W. and C.W.M.K. assisted in interpreting the EPR data. The computational studies were performed by C.B.Y. (ORCA, GAUSSIAN) and F.W. (TURBOMOLE). R.G.G. solved and refined the crystal structures. B.P. assisted the syntheses of compounds **1** and **2**. V. L. N. and R.K. has interpreted the magnetic properties of **8**. S.D. analysed the experimental and computational results. All authors co-wrote the paper.

Competing interests

The authors declare no competing interests.

Additional information

Supplementary information The online version contains supplementary material available at https://doi.org/10.1038/s41467-026-70910-5.

Correspondence and requests for materials should be addressed to Florian Weigend, Stefanie Dehnen, Rajesh G. Gonnade, Cem B. Yildiz or Moumita Majumdar.

Peer review information *Nature Communications* thanks Oriol Planas, and the other, anonymous, reviewer(s) for their contribution to the peer review of this work. A peer review file is available.